Lawrence Berkeley National Laboratory

Title
Location-Dependent Cobalt Deposition in Smartphone Cells upon Long-Term Fast-Charging Visualized by Synchrotron X-ray Fluorescence

Permalink
https://escholarship.org/uc/item/4dv3g477

Authors
Besli, Münir M
Usubelli, Camille
Subbaraman, Anantharaman
et al.

Location Dependent Cobalt Deposition in Smartphone Cells Upon Long-term Fast-charging Visualized by Synchrotron X-ray Fluorescence

Münir M. Besli,[1,2] Camille Usubelli,[1,3] Anantharaman Subbaraman,[1] Farshad Ramezan Pour Safaei,[1] Sharon Bone,[4] Christina Johnston,[1] Gerhard Schneider,[1,5] Francois Beauchaud,[1] Nikhil Ravi,[1] Jake Christensen,[1] Marca M. Doeff,[6] Michael Metzger,[7,]* Saravanan Kuppan[1,]*

[1]*Robert Bosch LLC, Research and Technology Center, Sunnyvale, California 94085, United States*

[2]*Dept. of Mech. Engineering, Karlsruhe Institute of Technology (KIT), Karlsruhe 76131, Germany*

[3]*Institute of Physics and Chemistry of Materials of Strasbourg (IPCMS), UMR 7504 CNRS, University of Strasbourg, Strasbourg Cedex 2 67034, France*

[4]*Stanford Synchrotron Radiation Lightsource, SLAC National Accelerator Laboratory, Menlo Park, California 94025, United States*

[5]*Materials Research Institute, Aalen University, Aalen 73430, Germany*

[6]*Lawrence Berkeley National Laboratory, Energy Storage and Distributed Resources Division, University of California, Berkeley, California 94720, United States*

[7]*Department of Physics & Atmospheric Science, Dalhousie University, Halifax B3H 4R2, Canada*

*Email: Michael.Metzger@dal.ca; Saravanan.Kuppan@us.bosch.com

Abstract

In this work we investigate the transition metal dissolution of the layered cathode material $LiCoO_2$ upon repeated fast-charging of three smartphone batteries from different manufacturers, using synchrotron micro X-ray fluorescence (µ-XRF). Using this spatially resolved technique, dissolution of Co and subsequent, location dependent, deposition on the anode is observed. µ-XRF mapping of selected parts of the anode electrode sheets, such as electrode folds and edges of the jelly roll, reveal the difference in the way Co is deposited on specific regions of the anode electrode. While some folds show no depositions, edges of the anode show gradually accumulating Co depositions. Careful quantification of the dissolved Co reveals that capacity loss scales with the amount of deposited Co on the anode; i.e., total Co loss from within the cathode. Soft X-ray absorption spectroscopy of the Co depositions on the anode shows that Co is mainly deposited in a reduced 2+ state. While optimization of the fast-charging protocol mitigates Li plating on the anode, no significant difference in the amount of deposited Co can be observed between an optimized and non-optimized fast-charging algorithm.

1. Introduction

Lithium cobalt oxide ($LiCoO_2$) is one of the most utilized cathode materials for Li-ion batteries within the ever increasing mobile consumer electronics market.[1,2] At upper cut-off voltages of 4.2 V (vs. Li/Li$^+$), $LiCoO_2$ delivers a usable specific capacity of 140 mAh/g corresponding to a composition x = 0.5 in Li_xCoO_2.[2–4] Due to the ever-increasing power and energy demand of mobile electronic devices such as smartphones, nowadays an upper cut-off voltage of 4.35 or 4.4 V for $LiCoO_2$ is typical in order to extract more capacity from the material.[2,5] However, at these high potentials, deteriorations of the cathode material can occur, leading to faster capacity decay, side reactions of the cathode with the electrolyte,[6] oxygen loss from within the crystal lattice,[7] and Co dissolution.[6,8] Many material scientists have contributed possible solutions to these problems over the years by introducing efficient surface modifications and dopants.[9–11] Although these efforts have paved the way towards using $LiCoO_2$ cathodes at higher potentials in mobile consumer applications, other strategies, such as optimized model-based charging protocols, are needed to enable fast-charging and mitigate the hastened degradation caused at higher rates.[12] Some protective charging algorithms are capable of avoiding low anode potentials that would otherwise cause Li plating. Typical degradation effects occurring during fast-charging can range from thermally accelerated side reactions to Li plating and mechanical effects such as particle decrepitation.[12] Furthermore, the interplay of these effects can also introduce other phenomena such as transition metal dissolution of the cathode,[12] especially at higher cut-off voltages, as it is typically believed to be related to electrolyte oxidation and subsequent generation of acidic species in the electrolyte that attack the cathode active material.[8,13,14] The application of a model-based, optimized fast-charging profile can help mitigate these types of degradation while providing consumers the freedom to charge their portable electronics in a short amount of time. While it has been shown previously that optimized fast-charging algorithms can enhance battery life cycle as well as reduce Li plating,[12,15–18] little information is available on the impact of fast-charging protocols on transition metal dissolution. Several

authors have investigated the general concept and effects of transition metal dissolution from layered cathode materials,[8,19–23] indicating how dissolution of transition metals from layered cathode materials can lead to capacity fade. Similarly, it is well established in the literature that higher upper cut-off voltages lead to increased amounts of dissolved transition metals.[22,24–26] While the dissolution and deposition of transition metals has been quantified using various techniques in literature, only a few studies are available that focus on the visualization of transition metal deposition on the negative electrode using techniques such as X-ray fluorescence (XRF). Noteworthy work has been published by Evertz et al. and Thompson et al. for NMC111 and NMC532, respectively, investigating the transition metal dissolution and deposition on the anode.[24,27,28] Similarly, analysis of the elemental distribution on the positive electrode, for cathode materials containing several transition metals, has also been studied using micro X-ray fluorescence (μ-XRF).[29,30] While the previously published work shows how powerful the (μ-)XRF method can be for elemental distribution analysis and also quantification purposes for different parts of a full cell, this technique has not been used to quantify distinct areas of electrodes which are spatially separated. In this regard, spatially separated regions include the center part, the folds of the jelly roll of the flat pouch-type cells and the overhang regions where the negative electrode extends beyond the positive electrode. Understanding the primary deposition locations of transition metals that are dissolved from the positive electrode can help improve future cell designs and allow a better understanding of how transition metal deposition occurs on the negative electrode of commercial cell phone batteries.

In this work, we seek to understand several questions related to the location dependent deposition of Co on the anode. Our main focus is to shed light on how optimized fast-charging algorithms, proven to be effective for reducing the amount of Li plating on the anode,[15,31] can influence the amount of transition metal dissolution, and how much of an influence the anode location within the cell has on the deposition of Co. For this, we used *ex-situ* synchrotron μ-XRF spectroscopy to probe harvested anode samples after two fundamentally different fast-charging protocols; an optimized fast-charging protocol derived using a

physics-based electrochemical model, and a fast-charging protocol suggested by the Original Equipment Manufacturer (OEM) of the smartphone. Previously, we reported the benefits of using an optimized charging profile and how Li plating can be prevented.[18] Our demonstration here focuses on the protocol induced differences in the amount and location of deposited Co on the anode and the differences in Li depositions on specific, spatially distinct locations such as edges, folds, and center parts of the negative electrode. We use three state-of-the-art smartphone cells from three different manufacturers to generalize our findings.

2. Results and Discussion

In the first part, we discuss the implementation of a model-based, optimized fast-charging algorithm based on a physics-based electrochemical model. The tested $LiCoO_2$ smartphone batteries are from three different cell manufacturers and are currently employed in state-of-the-art smartphones; hereafter, we refer to the cells as cell type A, B, and C (also see Table 1 in the experimental section). After full parameterization of each specific battery we developed a complex physics-based electrochemical model for control algorithm synthesis for each cell type A, B, and C; details on this procedure are disclosed in a US filed patent application.[32] From this starting point, we derived an optimal charging profile for each cell type, which is constrained to current, voltage, and temperature limits specified by the specific cell manufacturer, i.e., our optimized charging profile stays within these limits but achieves similar or faster charging with the same or less aging. As the cell ages, the optimal fast-charging profile is adjusted to the cell's state of health (SOH) using proprietary adaptation rules and custom building blocks for charging profile generation.[33] The building blocks for approximation of the new fast-charging profile include, among others, constant current (CC), ramp current, constant voltage (CV), and ramp voltage, while adaptation criteria could be based on state of charge (SOC), SOH, current, voltage, temperature, capacity, and so forth.[18,34]

Using the optimized charging profile for each cell type (hereafter referred to as *MOD*$_{cyc}$, *model-based cycling protocol*) and the cycling profile specified by each OEM (hereafter referred to as *OEM*$_{cyc}$, *OEM-based cycling protocol*), we conducted long-term cycling (details on the cell specific cycling parameter limits can be found in Table 1) to assess the differences in capacity retention between the MOD_{cyc} and OEM_{cyc} profiles. Note that OEM_{cyc} refers to the specific cell type's OEM specified cycling protocol and MOD_{cyc} to an individually derived cycling protocol for each cell type. Figure 1 shows the normalized charge capacity over lifetime for the three different cell types when cycled with the specific OEM_{cyc} profile (red) and the MOD_{cyc} profile (blue). For cell type A, the MOD_{cyc} charging protocol was shown to

be beneficial with a capacity retention of 87.1% (84.2% when using the OEM_{cyc} profile) after 700 cycles, but cell type B showed approximately the same performance under both charging protocols with capacity retentions of 88.1% and 88.5% for MOD_{cyc} and OEM_{cyc} after 800 cycles, respectively. Besides this observation, one major finding is the drastic capacity decay observed for cell type C after only 115 cycles. Although the MOD_{cyc} profile seems to be more beneficial for cell type C with a capacity retention of 93.5%, compared to cell type A and B, the capacity retention with the OEM_{cyc} protocol is much worse (82.1%). Finally cell type C exhibited severe capacity fade under both charging conditions after only 115 cycles. Nevertheless, the MOD_{cyc} profile provided significant benefit with a capacity retention of 93.5%, vs. 82.1% for the OEM_{cyc} protocol.
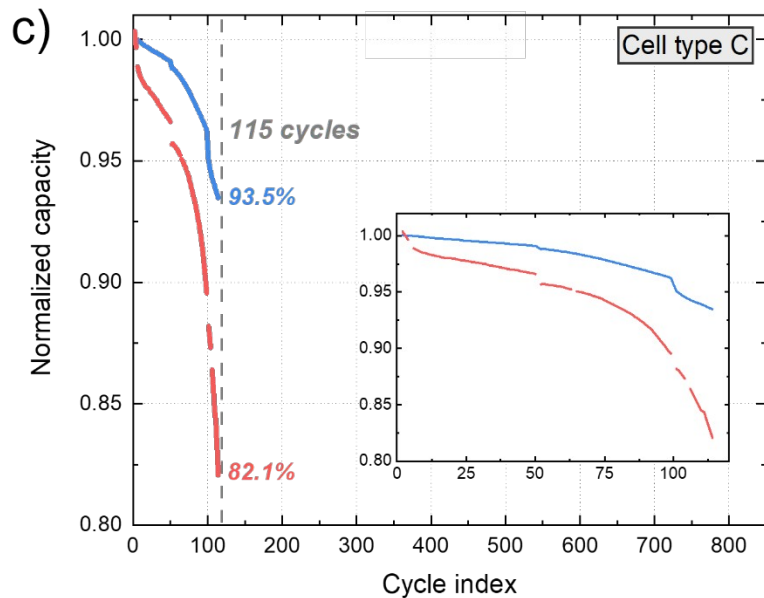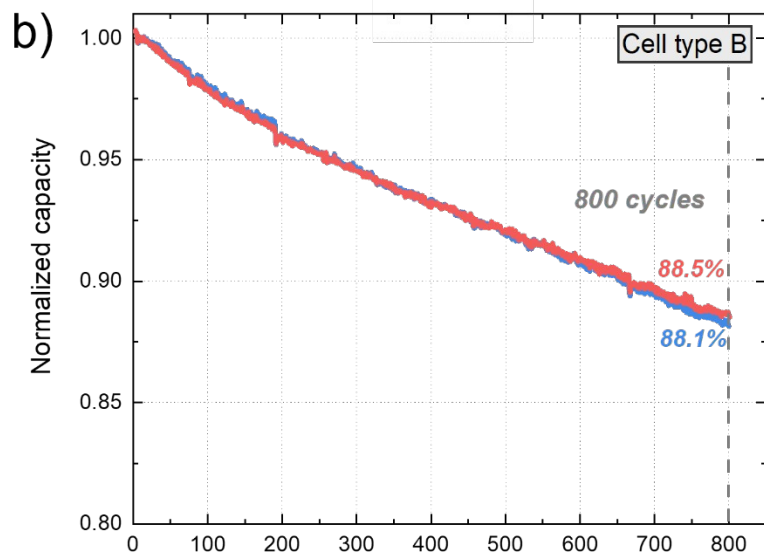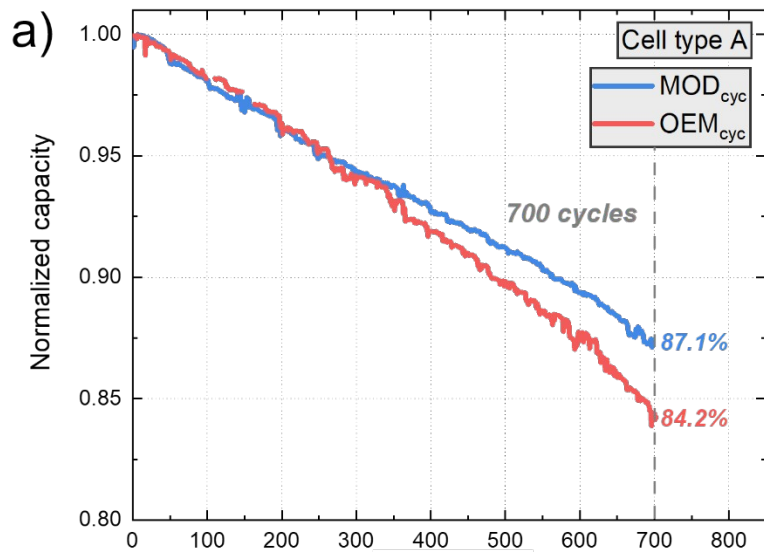
Figure 1: (a-c) Capacity retention of three different $LiCoO_2$ smartphone cells (type A, B and C) under the specific MOD_{cyc} charging protocol (blue) and the OEM_{cyc} (red) charging protocol.

Post-mortem analysis of all three cell types, after cycling with their respective OEM_{cyc} protocol, reveals a tremendous difference between the amounts of Li deposited on the anode on a macroscopic scale. While cell types A and B only had minimal Li depositions, primarily around the folds and edges of the negative electrode jelly roll, almost all of the anode in cell type C was covered with Li depositions and electrolyte decomposition products (Figure 2, see also our previous work analyzing in detail the nature of the anode deposits for this cell type).[18] At the same time, cell type C showed almost no Li depositions or any Li plating[a] when cycled with the MOD_{cyc} protocol. In general, Li deposition and plating on the graphite anode is thermodynamically enabled when the anode surface potential (vs Li/Li^+) becomes negative.[35,36] The voltage polarization and deviance from the thermodynamic equilibrium potential is a combined result of various effects such as Ohmic drop and diffusion overpotentials.[37] Cell type C's OEM_{cyc} protocol most likely manages the anode surface potential in a non-optimized way (e.g., due to inadequate parameterization of the model or effects that are not considered, e.g., local mechanical effects) and hence triggers the deposition of Li, while for cell type A and B, under both fast-charging protocols OEM_{cyc} and MOD_{cyc}, this can be prevented. From the different amounts of Li depositions for cell type C after OEM_{cyc} and MOD_{cyc} protocol, one can say, that an optimized fast-charging profile and the continuous adaption and refinement of this profile over the lifetime of the cell can be advantageous for the lifetime of $LiCoO_2$ smartphone batteries. However, as seen for both cell type A and B, a refined cell chemistry and an optimized fast-charging profile play crucial roles for the cell performance and lifetime by inhibiting a negative anode surface potential and hence Li deposition and plating.

---

[a] As in Waldmann et al.,[37] the term 'Li plating' is used when Li homogeneously covers the electrode surface, and 'Li deposition' is used for the thick macroscopic morphologies corresponding to local hotspots or Li at the edges or folds of the negative electrode.
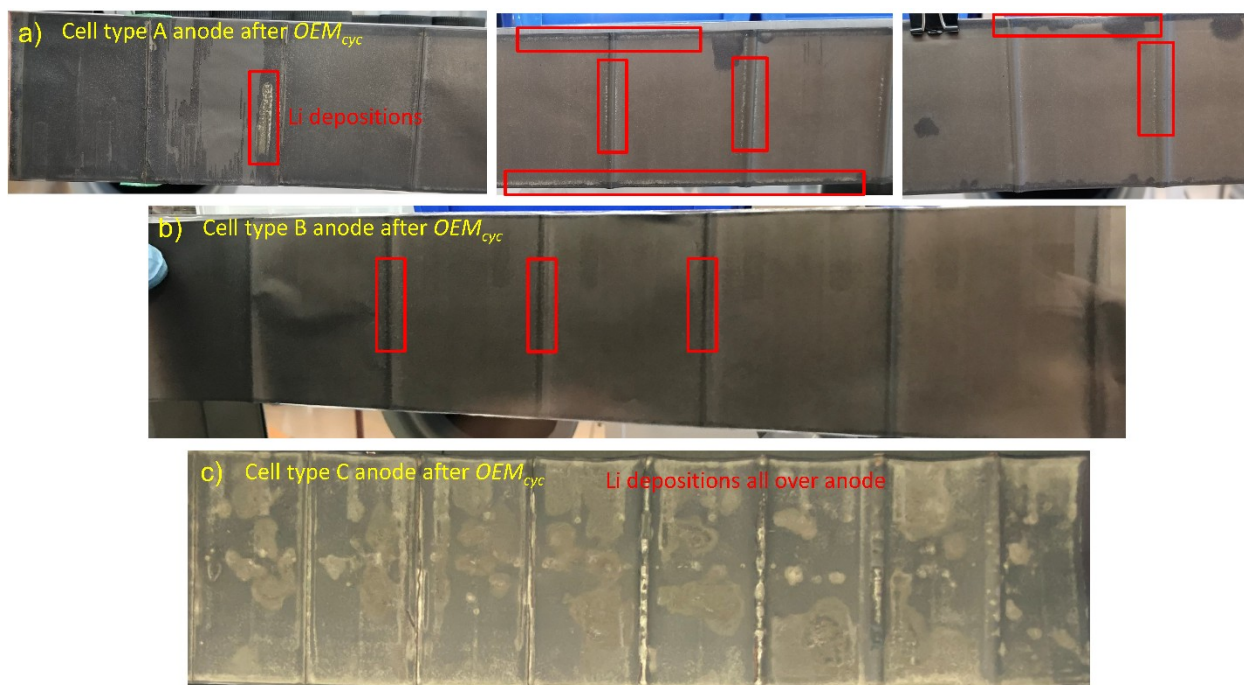
Figure 2: (a-c) Harvested anodes from cell type A, B, and C after OEM_{cyc} protocol, respectively. While only a few Li depositions were found on the edges and folds of cell type A and B, large Li depositions and electrolyte decomposition products on the entire anode were observed for cell type C.

A close look at the anodes of cell type A after cycling with the OEM_{cyc} protocol (see Figure 2a and supplementary Figure S1) shows that large local Li depositions are formed mainly around the folds and edges, while a few isolated Li deposition sites are located within the center regions (corresponding to the tab location). In Figure 3, scanning electron microscopy - energy-dispersive X-ray spectroscopy (SEM-EDX) was used to study the distinct sites in greater detail. The exemplary sites of Li deposition, as observed for cell type A and B within the center, around the folds, and the edges, referred to as sites 1, 2, and 3, respectively, are marked in supplementary Figure S1 for cell type A. Figure 3 shows the differences in the chemical compositions for these sites for cell type A observed with SEM-EDX. A number of O-rich deposits are detected on some of the center parts and edges of the anode cycled with the OEM_{cyc} protocol. For anodes harvested after MOD_{cyc} protocol, fewer O-rich deposits are visible in the center parts, the folds, and edges of the anode compared to those cycled with the OEM_{cyc} protocol. The

observed oxygen signal in the SEM-EDX analysis serves as indirect evidence for Li depositions: Upon exposure of the harvested graphite anodes to ambient conditions and immediate analysis via X-ray diffraction (XRD), a transformation of the Li depositions to lithium hydroxide (LiOH) occurs (supplementary Figure S2). Analysis with Raman spectroscopy revealed that part the Li deposits, or LiOH, might also convert to lithium carbonate (Li_2CO_3).[38] Similarity of the deposits to common compounds of which the solid electrolyte interphase (SEI) is made of was also checked for using Raman spectra reported in the literature (for a detailed explanation see supplementary Figure S2); little to no similarity to common SEI compounds was found. The observed oxygen signal in the SEM-EDX can be directly and semi-quantitatively correlated with the amount of Li depositions, which is shown in supplementary Figure S3. Here, the exact locations shown in Figure 3 were quantified using ImageJ v1.52a,[39] where the total area was used and compared to the area covered with O-rich depositions, serving as a semi-quantification of the deposition area. A comparison of the center parts (site 1) of anodes harvested from cell type A after both protocols OEM_{cyc} and MOD_{cyc}, indicates that the total area covered by depositions is twice as high after OEM_{cyc} fast-charging. This is also true for the fold regions (site 2). Interestingly, for the edge regions (site 3) of cell type A, only 0.25% of the total area is covered by depositions when the MOD_{cyc} fast-charging protocol is used, while 26.5% of the analyzed total edge area is covered by O-rich depositions after the OEM_{cyc} fast-charging protocol. Combining the macroscopic observations indicates that Li deposits form primarily in edge and fold locations of the cell where compression, electrolyte, and current distributions are expected to be most heterogeneous. This is in good agreement with the literature, where it was shown that Li deposits preferentially at electrode edges due to geometric effects[40] and electrode nonuniformities,[41] heterogeneous pressure[42] and compression,[43] and higher current densities.[44] Another observation confirming this is Figure 2c, showing the depositions on the anode of cell type C after the OEM_{cyc} protocol; here all folds and edges are fully covered in Li depositions and decomposition products of the electrolyte, while the center parts of the electrodes are not fully covered by depositions.
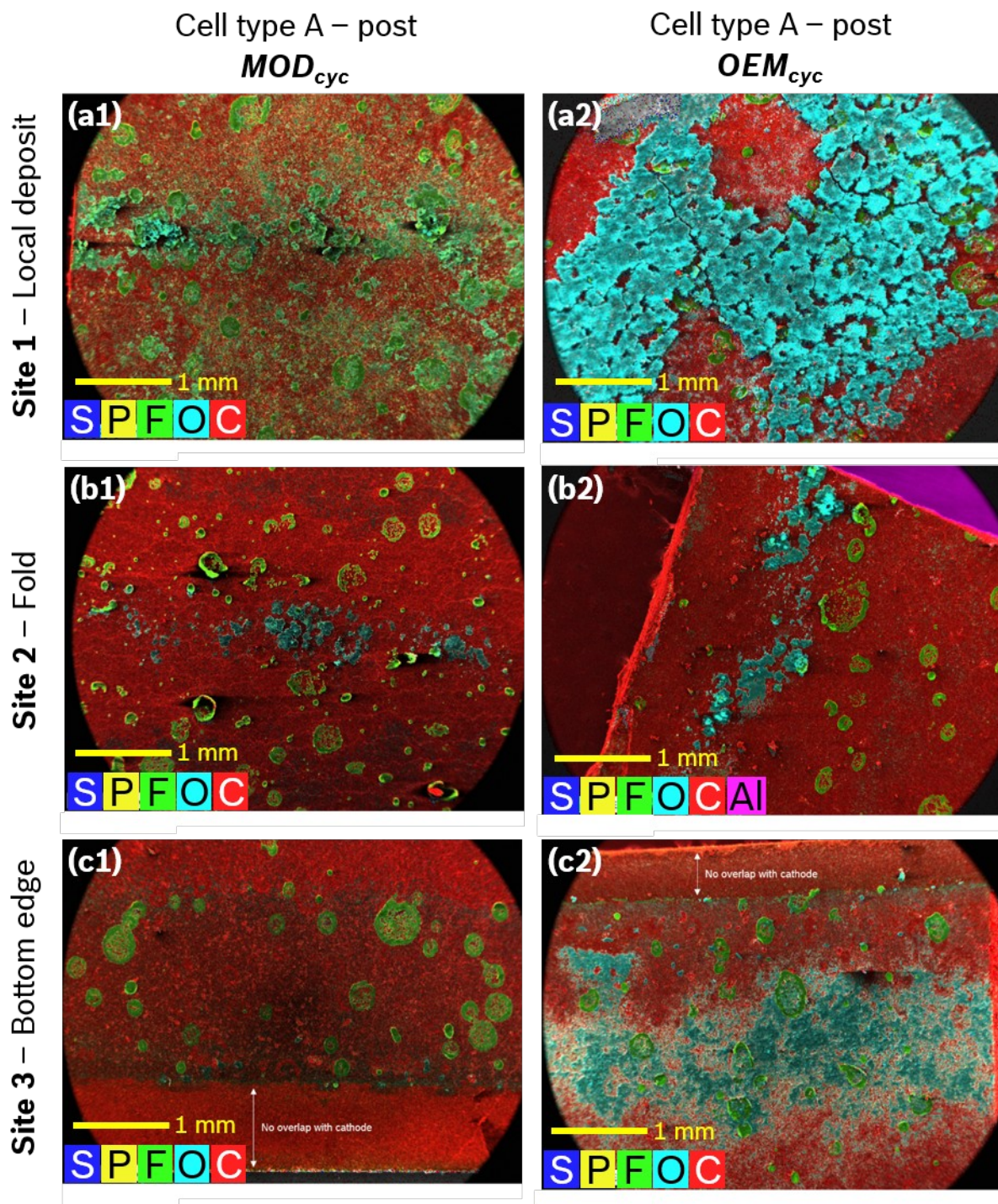
Figure 3: SEM-EDX analysis of three sites on the negative electrode harvested from cell type A after MOD$_{cyc}$ (a1-c1) and OEM$_{cyc}$ charging (a2-c2). O-rich depositions highlighted in the cyan area likely result from the conversion of metallic Li depositions to LiOH and Li$_2$CO$_3$ upon exposure to ambient conditions,

and serves as an indirect measure for the amount of Li depositions on the specific sites 1, 2, and 3, namely, center, fold, and edge.

After visual and microscopic localization of the most predominant Li deposition sites, harvested anodes of pristine cells and cells after MOD_{cyc} and OEM_{cyc} fast-charging protocols were further analyzed with synchrotron μ-XRF in order to quantify the degree and location of deposited Co on the anode (see Figures 4-6). The focus of the μ-XRF study is the spatial visualization of the deposition of dissolved Co from the cathode onto the anode and the quantification of Co on the deposition sites. An average concentration, reported in $μg/cm^2$, was obtained for the different parts of the electrodes (center, fold, edge) as seen in supplementary Figure S4. Furthermore, the total amount of Co deposited on the anode is extrapolated from the average concentrations of Co of the center regions for each cell type and charging protocol (plus pristine; see Figure 7a).

Pristine anodes of all three cell types did not show any significant amount of Co deposition on a $μg/cm^2$ level as seen in panels a-c of Figures 4, 5, and 6. Minimal Co deposition is visible only around the folds and the bottom edge of cell type A (Figure 4b and 4c, respectively), shortly below the area where the cathode overlaps with the anode. The actual anode overhang that does not overlap with the cathode, due to the fact that it is slightly oversized, does not show any significant Co deposition (Figure 4c). Quantitatively, the average Co concentrations on the center part of the pristine anodes were 3.23 ± 1.35 $μg/cm^2$, 3.32 ± 0.97 $μg/cm^2$, and 3.07 ± 0.48 $μg/cm^2$, for cell type A, B, and C, respectively (see Figure S4). These concentrations are 2 to 3 times lower than the concentrations for the corresponding center parts after MOD_{cyc} and OEM_{cyc} protocols. This may be a result of calendar aging, as the battery might have been stored for several months under uncontrolled conditions, and/or variations in the manufacturer specified formation of the cells, which were not disclosed.
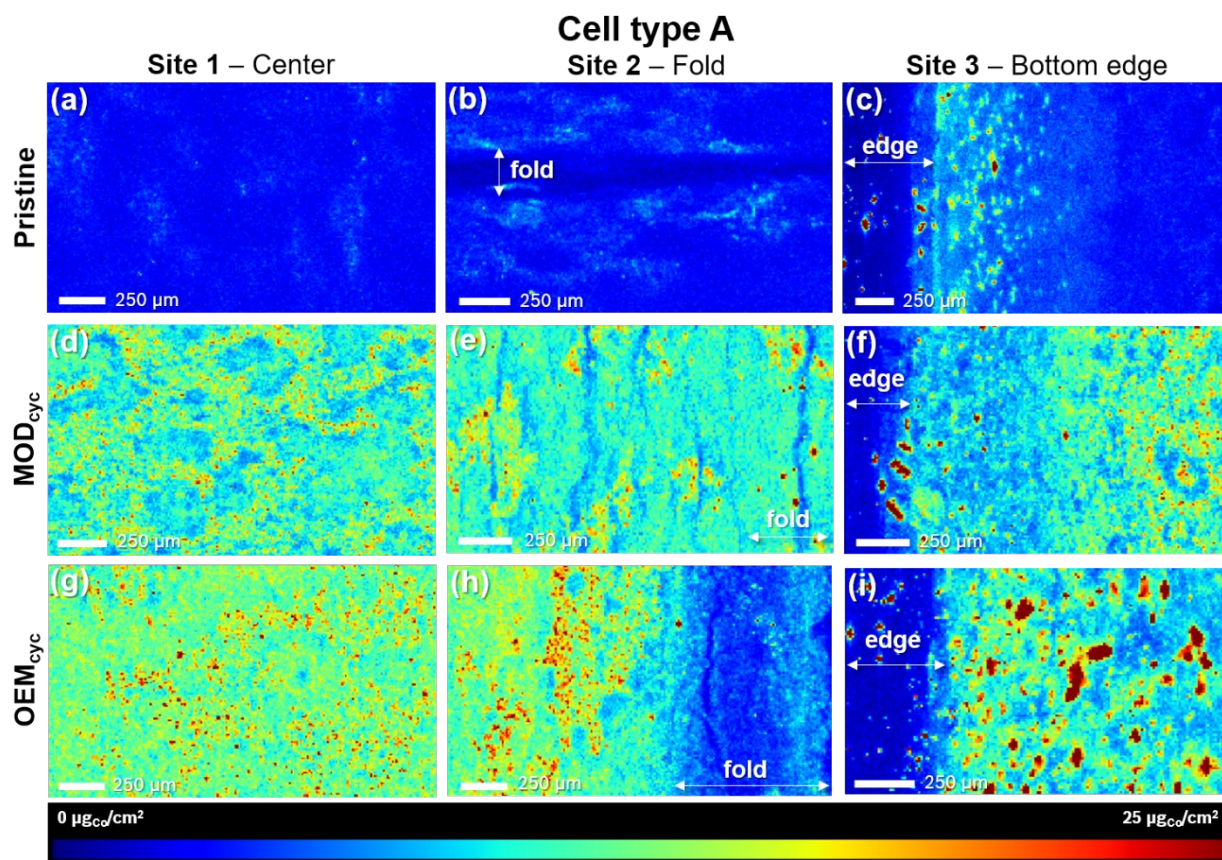
Figure 4: Synchrotron μ-XRF results for cell type A with Co deposits color-coded according to the depicted color map at the bottom (blue and red represent low and high Co concentrations, respectively). (a-c) Visualization of Co depositions on the anode of a pristine cell for sites 1-3 (center, fold, and bottom edge). (d-f) Visualization of Co depositions on the anode after MOD_{cyc} fast-charging protocol for sites 1-3. (g-i) Visualization of Co depositions on the anode after OEM_{cyc} fast-charging protocol for sites 1-3.

Interestingly, a fairly homogeneous deposition of Co is observed for the center regions of cell type A's anode after both the MOD_{cyc} and OEM_{cyc} protocols, with the appearance of greater deposits on the anode cycled with the OEM_{cyc} protocol compared to the MOD_{cyc} counterpart. This appears to be true not only for the center regions, but also the edge of cell type A's anodes when comparing Figure 4f and 4i; the higher concentration of Co is specifically visible in the Co hotspots as seen in Figure 4i. However, a quantitative comparison of the average deposited Co concentration on the center parts of MOD_{cyc} (11.39 ± 5.94 μg/cm^2) and OEM_{cyc} (12.78 ± 3.51 μg/cm^2) anodes reveals only a small difference that is not statistically

significant (see supplementary Figure S4). Conversely, the folds of cell type A after the MOD_{cyc} protocol show the opposite effect and a statistically significant difference for the Co deposition (Figure 4e and h). Here, after OEM_{cyc}, the fold regions only a small amount of Co deposition (4.80 ± 1.32 µg/cm^2), while the average concentration of Co on the folds after MOD_{cyc} protocol is 10.18 ± 2.14 µg/cm^2 (see supplementary Figure S4).

The observation that there is no statistically significant difference between the amount of Co deposited with both cycling protocols also holds true for the center parts and edges of cell type B and C, although it appears that there is a small concentration difference in the µ-XRF maps for the center parts and edges between anodes harvested after MOD_{cyc} and OEM_{cyc} fast-charging protocols (Figure 5 and 6, cell type B and C, respectively). Quantitative analysis of the obtained maps shows that there is no statistically significant difference between the amount of Co deposited on the center parts of the anodes by the two different fast-charging protocols (see supplementary Figure S4). However, this is not true for cell type C's edge region since the OEM_{cyc} protocol results in less plating of Co (4.14 ± 1.17 µg/cm^2) than the MOD_{cyc} fast-charging protocol (7.66 ± 2.29 µg/cm^2). One noteworthy difference is that, in contrast to cell type A, where the fold regions after the MOD_{cyc} protocol are covered with Co deposits, and the fold region after the OEM_{cyc} protocol are free of deposits, cell type B shows the exact opposite trend (Figure 5e and h); here, the folds after MOD_{cyc} are free of deposits, while the folds after OEM_{cyc} are fully covered in Co. Similarly, compared to the very homogenous deposition of Co on the center parts of cell type A, cell type B's anodes show a more inhomogeneous distribution of Co, which holds true for the center, although not for the folds or edges.
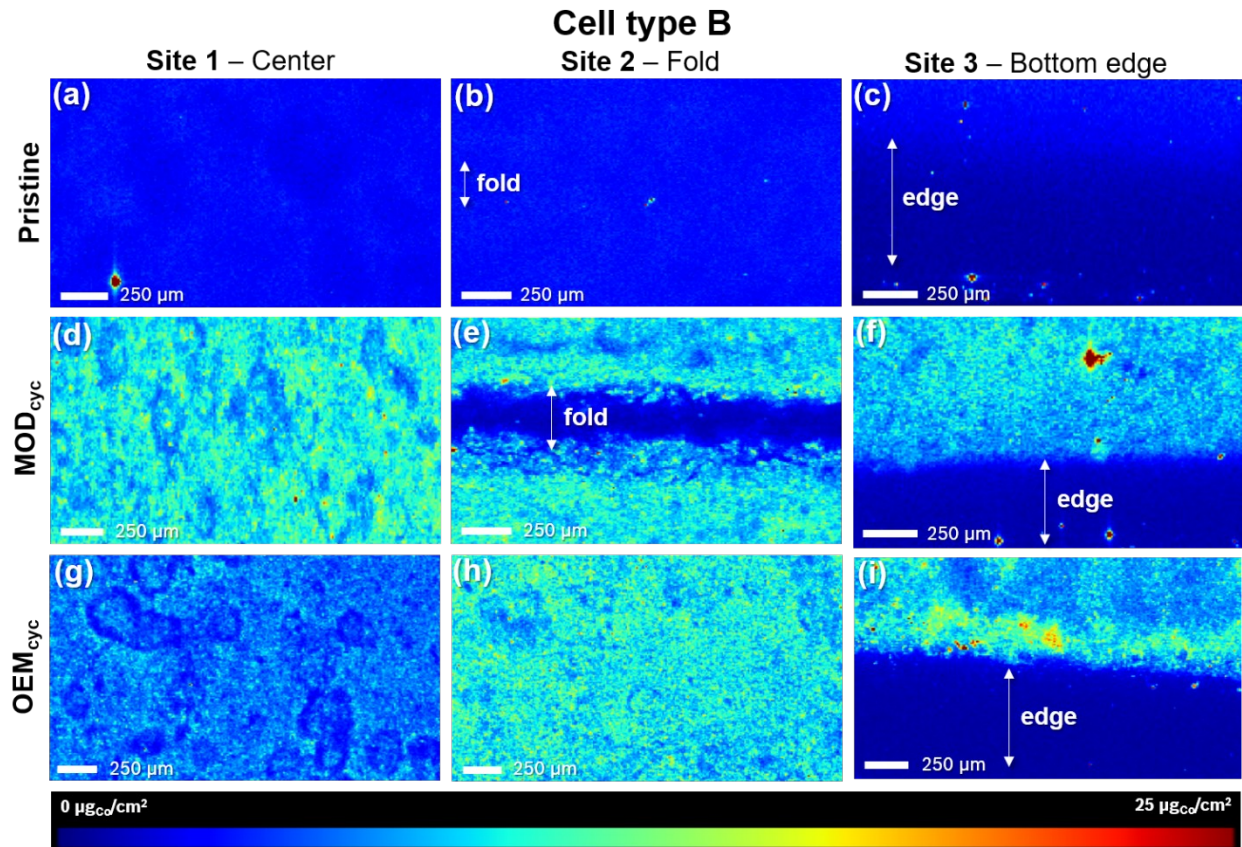
Figure 5: Synchrotron µ-XRF results for cell type B with Co deposits color-coded according to the depicted color map at the bottom (blue and red represent low and high Co concentrations, respectively). (a-c) Visualization of Co depositions on the anode of a pristine cell for sites 1-3 (center, fold, and bottom edge). (d-f) Visualization of Co depositions on the anode after MOD_{cyc} fast-charging protocol for sites 1-3. (g-i) Visualization of Co depositions on the anode after OEM_{cyc} fast-charging protocol for sites 1-3.

Lastly, for cell type C, the exact location of the folds seem to be mostly free of Co deposits after both fast-charging algorithms. Cell type C is the only cell with a full metal casing, i.e., very rigid, compared to cell type A and B's polymer pouch material. The expansion and contraction of the jelly roll during cycling leads to higher mechanical tension in the folds during charging, possibly squeezing electrolyte out of the fold regions. In this electrolyte deficient region, dissolved Co cannot reach the anode. Likewise, the overhang regions of the anode are expected to be drier than areas where the anode faces the cathode. Although all cells are tightly packed pouch cells, the very stiff metal casing of cell type C might compress

the entire cell stack in a different way than a more flexible polymer pouch, and hence squeeze out more electrolyte from the fold regions; with less electrolyte being present in the folds, Co dissolved in the electrolyte cannot deposit on those regions. For cell type A and B, this seems to happen only for folds in which the central radius is small, i.e., the fold is located within the very first windings of the prismatic winded pouch cell stack (Figure 5e). In some instances, however, also folds with broader radii (Figure 4h) seem to be free of Co deposits, and hence it is unclear, if the same reasoning of electrolyte deficiency due to rigid compacting, as observed for cell type C with the metal jacket, is applicable for all folds of the cells wrapped in the polymer pouch material. We hypothesize that it will strongly depend on the amount of cell swelling during cycling as well as the cell radii, whether Co will be deposited on the folds of the graphite anode or not. From our observations in Figure 4-6, one would not expect Co depositions in the majority of graphite anode folds due to compression and subsequent electrolyte loss from the fold regions. With this in mind, it is also very difficult to establish a correlation between locations of Li deposits and Co deposits. While Li deposits are preferentially located at electrode edges and folds as described above, the deposition of Co seems to be strongly affected by, among others, local electrolyte deficiency and cell radii.

The anode edges of cell type C also show a very interesting pattern, in which a high-low-high Co concentration gradient is visible after MOD_{cyc} charging (Figure 6f), while after OEM_{cyc} (Figure 6i) a low-high concentration gradient (starting at the edge and moving inside) is obtained. A comparable concentration gradient is also observed for cell type A's anode edge after the MOD_{cyc} fast-charging protocol (Figure 4f); only cell type B shows a very homogenous deposition of Co on the edges without a significant gradient. In a comparable fashion to the concentration differences observed on the folds, this is possibly also a result of inhomogeneous electrolyte wetting on the edges. A schematic overview of the different concentration gradients are shown in supplementary Figure S5.
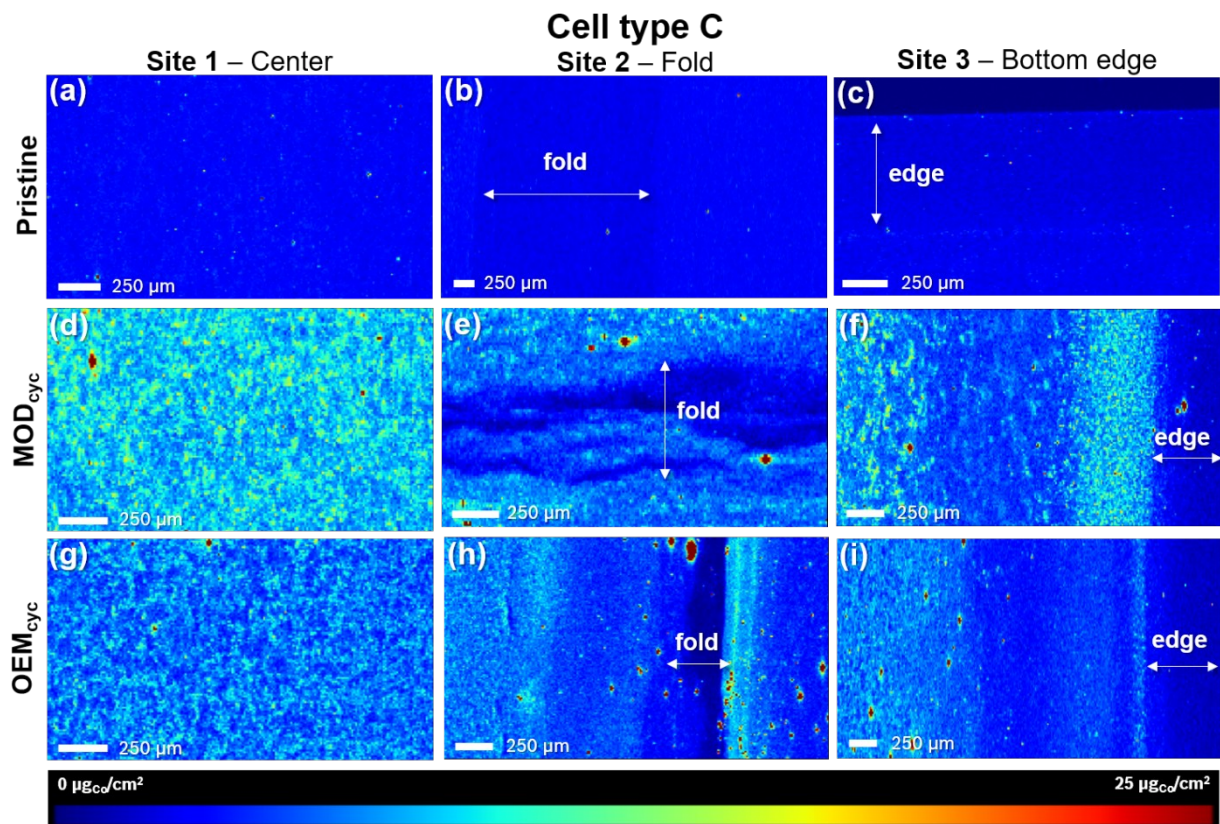
Figure 6: Synchrotron µ-XRF results for cell type C with Co deposits color-coded according to the depicted color map at the bottom (blue and red represent low and high Co concentrations, respectively). (a-c) Visualization of Co depositions on the anode of a pristine cell for sites 1-3 (center, fold, and bottom edge). (d-f) Visualization of Co depositions on the anode after MOD_{cyc} fast-charging protocol for sites 1-3. (g-i) Visualization of Co depositions on the anode after OEM_{cyc} fast-charging protocol for sites 1-3.

The average Co concentration obtained for the center parts of the anodes for each cell type after both fast-charging protocols and pristine cells was further used to extrapolate the total amount of deposited Co using the total anode area, as determined during cell opening (Figure 7a). It is found that the total amount of Co lost from the cathode and deposited on the anode is on the order of a few milligrams, with pristine cells showing a total loss of 3.24, 3.70, and 2.33 mg, MOD_{cyc} fast-charged cells showing 11.41, 10.32, 6.31 mg, and OEM_{cyc} fast-charged cells showing 12.80, 6.55, and 4.63 mg total Co loss for cell type A, B, and C, respectively. As mentioned earlier, all pristine cells show a 2-3 times lower concentration with a

very narrow statistical uncertainty. In contrast to this, the cells after fast-charging show a higher, very similar concentration and a high uncertainty, resulting in very little difference in the amount of deposited Co between the protocols for all three cell types. Hence it is not possible to say which fast-charging protocol causes higher Co loss from the cathode and subsequent Co deposition on the anode. For example, for cell type A the OEM_{cyc} protocol shows a slightly higher average deposition of Co, while for cell type B and C, the MOD_{cyc} protocol shows a higher Co deposition, however, with high statistical uncertainty. Ultimately, the quantified amounts of Co on the anode, after both fast-charging protocols, are very similar and independent of the cell type.

To complement the quantitative μ-XRF results, synchrotron soft X-ray absorption spectroscopy (soft XAS) was employed, and shows that the Co deposited on the anode is in a reduced valence state of 2+ as seen in supplementary Figure S6.[45] Although $LiCoO_2$ is active between a valence state of 3+ and roughly 3.5+ at x = 0.5, here, dissolved Co is deposited as 2+ on the anode after reduction via electrolyte oxidation. This result is in very good agreement with what has been previously reported in the literature. Wandt et al. had already observed Co^{2+} depositions on the anode using K-edge X-ray Absorption Near Edge Structure (XANES) spectroscopy.[25] Given the fact that the redox potential of Co/Co^{2+} (2.52 V (vs. Li/Li^+) in a typically utilized Li-ion battery,[46] and 2.77 V (vs. Li/Li^+) in aqueous media[47]) is above the potential for electrolyte reduction and that of the graphite anode, one would expect metallic Co deposits on the anode,[25,46] as has been variously described in the literature.[6,13] These deposits of Co in its metallic state then act as a catalytic center for further electrolyte reduction, leading to decomposition products on the anode. To explain the presence of Co^{2+} on the anode, two theories can be considered: (I) Jung et al. have postulated that dissolved transition metals, such as Co^{2+}, are probably first electrochemically deposited in their metallic state, but subsequently re-oxidized by reacting with SEI, causing damage to the SEI and further decomposition products;[46] (II) Wandt et al. have suggested that Co might be immobilized

in the +2 oxidation state in the outer SEI at a greater distance to the actual graphite surface, hence preventing the reduction of Co^{2+} to the metallic state.[25]

In addition to the observation of Co^{2+}, another question that arises is how the total amount of deposited Co^{2+} influences depositions arising from Li and electrolyte decomposition; as seen in Figure 2, cell type A and B show minimal electrolyte decomposition products and Li deposits, but have, on average, higher amounts of total deposited Co on the anode (Figure 7a). Although the differences in the total amount of Co between the different cell types might not be statistically significant, the total amount of Co was found to be the lowest for cell type C. However, the calculated total amount of Co for cell type C evolved fairly quickly within 115 cycles compared to more than 700 cycles for cell type A and B. With this, it is difficult to judge the magnitude of the detrimental effect of deposited Co, which may enhance Li deposition and further electrolyte decomposition.
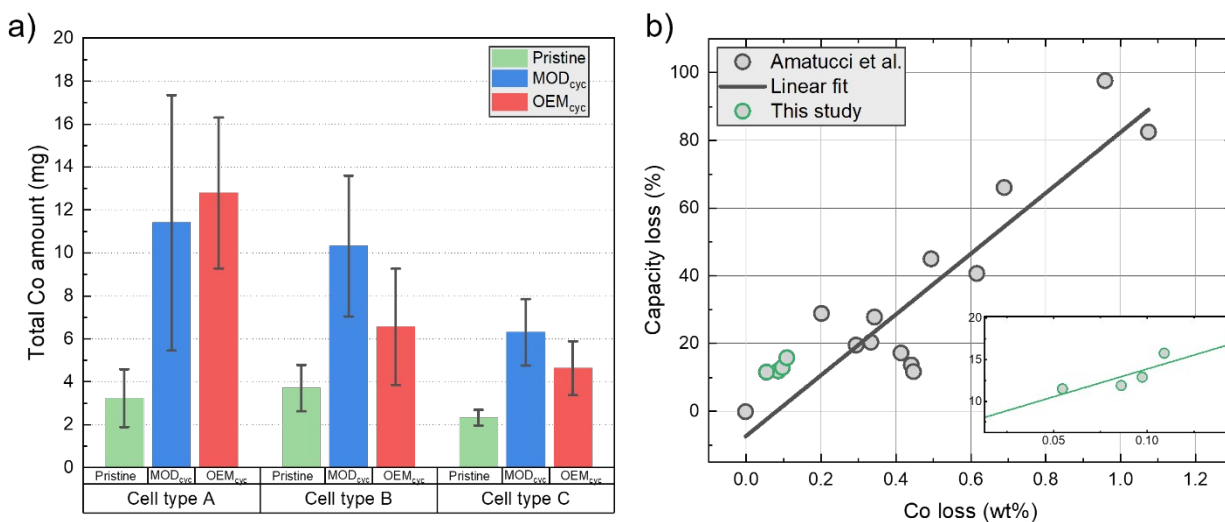

Figure 7: (a) Total deposited Co amount in mg on the entire anode area for pristine cells (green), cells after MOD_{cyc} (blue), and cells after OEM_{cyc} (red) fast-charging protocol. For the calculation of the total Co amount, the deposited average Co concentration on the center parts of the anode and the total anode area, as measured while opening the cells, was used. Error bars represent the standard deviation. (b) Linear correlation (black) of the lost capacity with the amount of deposited Co (in wt%) with data from

Amatucci et al.[8] Green data points represent the data presented in this study with a linear fit for the data points shown in the inset.

Finally, with the intention of finding a relationship between the amount of deposited Co on the anode and the lost capacity, the retained capacities (Figure 1) are plotted against the wt% of deposited Co on the anode (Figure 7b). It should be noted that the acquired results for cell type C are not considered into this relation, due to the significantly lower number of cycles and markedly poorer cycling performance compared to cell type A and B (see Figure 1), but most importantly, due to the proportion of capacity loss as a result of Li depositions (Figure 2c). Taking only cell type A and B into account, this gives a tangible estimate about the total Co amount that is lost from the cathode and the lost capacity; however, the long cycle life makes it challenging to obtain more data points to extend this relationship. Hence, our results are compared against a study from Amatucci et al.,[8] in which $LiCoO_2$ materials, with different cycling efficiencies, were cycled against a Li anode. Although the relationship between the lost capacity and lost/deposited Co in the named study was established for different samples of $LiCoO_2$ with a variety of cycling efficiencies related to the extent of thermal annealing, it can be compared with the developed relationship presented here. The similarity in the linear fit confirms that, at least for cells without significant amounts of Li deposition, the deposition of Co on the anode is involved in the capacity fade mechanism, possibly by reducing the effectiveness of the SEI and accelerating the rate of electrolyte decomposition.

3. Conclusions

Application of synchrotron μ-XRF for qualitative and quantitative analysis of Co, dissolved from the cathode and deposited on the graphite anode, was demonstrated for state-of-the-art $LiCoO_2$ smartphone cells. A comparison of cells from three different smartphone manufacturers after fast-charging with an optimized electrochemical model-based protocol and the standard OEM-based protocol showed only minimal, insignificant differences in the amount of deposited Co by the two, fundamentally different, fast-charging protocols. The absence of Co in some folds of the anode and concentration gradients of deposited Co, specifically at the edges of the anodes, were revealed and correlated to possible heterogeneities in electrolyte content. Quantified losses of Co from the cathode were found to match the capacity loss in cells in which no substantial Li deposits were found on the anode. Soft XAS revealed that the Co deposits are mainly in a reduced valence state of 2+, possibly due to reduction of dissolved Co species through electrolyte oxidation. Although no tangible difference in deposited Co by two different fast-charging algorithms was observed, the optimized fast-charging algorithm revealed to be of crucial benefit for one cell type in which no Li deposits were observed with the optimized fast-charging protocol, and the whole anode was covered by Li deposits when the OEM-based protocol was employed.

4. Experimental

Electrochemical cycling

Two charging protocols were used for all three cell types. The standard charge is a CC-CV (constant current – constant voltage) protocol with a constant current $I_{max, charge}$ (see Table 1), and a CV hold at 4.4 V (referred to as OEM_{cyc}); each cell type was fast-charged with the respective protocol of the cell manufacturer. The model-based charging protocols (MOD_{cyc}) rely on minimizing certain aging indicators through the charging stage while simultaneously minimizing the time required to fully charge the battery, i.e., as the cell ages, the optimal fast-charging profile is approximated using simple building blocks for profile generation and adaptation rules to match the aged state of the cell. For each specific cell type, an individual MOD_{cyc} protocol is derived. More information on the exact derivation and cycling procedure of the MOD_{cyc} protocol can be found in a US filed patent application and a detailed study.[18,32] All tests were performed using an Arbin BT2000 tester and in a controlled temperature environment at 25 °C. Our battery tester has current/voltage accuracy of 0.02%. In order to access the cell terminals the battery Protection Circuit Boards (PCBs) were removed.

Cell Type A	
Chemistry	LCO/graphite
Capacity	3.2 Ah
E_{max}	4.4 V
E_{min}	3.0 V
$I_{max, charge}$	3.2 A (1 C)
Cell Type B	
Chemistry	LCO/graphite
Capacity	3.2 Ah
E_{max}	4.4 V
E_{min}	3.0 V
$I_{max, charge}$	3.2 A (1 C)
Cell Type C	
Chemistry	LCO/graphite
Capacity	2.7 Ah

E_{max}	4.4 V
E_{min}	2.7 V
$I_{max, \, charge}$	3.1 A (1.15 C)

Table 1: Specifications of three commercial smartphone cells from different suppliers.

Cell teardown

Prior to cell teardown and harvesting of electrode sheets, all cells were discharged with a C/20 rate to the respective cut-off voltage. Cells were transferred into an Ar-filled glove box (O_2 < 0.1 ppm, H_2O < 0.1 ppm) after removal of the battery protection circuit board (only cell type C). Transferred cells were carefully cut open using a ceramic knife (metal jacket of cell type C was carefully removed using electrically insulated pliers). The electrode stack was carefully opened and, after removal of the separator, the anode and the cathode were separated and dried in the vacuum antechamber overnight to remove residual electrolyte.

X-ray diffraction analysis

X-ray diffraction patterns of harvested anodes were obtained using a Bruker D8 ADVANCE X-ray diffractometer equipped with a Cu K-α radiation source and a Bruker LYNXEYE XE detector. The accelerating voltage and current were set to 40 kV and 40 mA, respectively. All scans were collected between 20 and 60° (2θ) at step size of 0.03° and a 1 sec/step. All samples were rotated at a 10°/min rotation speed. Background correction for all gathered XRD spectra was done using the Bruker DIFFRAC.EVA v4.2.1.1 software suite.

Raman spectroscopy

Raman spectroscopy was performed on a Horiba Scientific LabRAM HR Evolution Raman microscope equipped with a 405 nm diode laser, a 1800 grooves per mm grating, and a Synapse Open-Electrode CCD detector. The 405 nm laser was focused using a 50 x magnification lens, a numerical aperture (NA) of 0.5, and a field number of 26.5. A backscattering geometry was used to collect the scattered radiation. Rayleigh-scattered light was rejected using a filter.

Scanning electron microscopy-energy dispersive spectroscopy

Scanning electron microscopy - energy dispersive X-ray spectroscopy was conducted using a JEOL JSM-7200F Field Emission Scanning Electron Microscopy equipped with an Oxford X-Max^N 50 Silicon Drift Detector system. SEM imaging was performed using an accelerating voltage of 5 kV at medium probe (5-7) currents using the secondary electron detector. EDX was conducted using an accelerating voltage of 20 kV at high probe currents (10-14).

Synchrotron micro X-ray fluorescence spectroscopy

Synchrotron micro X-ray fluorescence analysis of harvested anodes was conducted at beam line 2-3 at the Stanford Synchrotron Radiation Lightsource (SSRL), a division of the SLAC National Accelerator Laboratory. A Kirkpatrick-Baez system was used to focus the beam down to a spot size of 2 x 2 μm^2. Detection was achieved with a Vortex silicon drift detector. Large anode areas of approximately 2 x 2 mm^2 size were mapped with X-rays of considerably smaller spot size (factor 10^6 difference) in order to achieve a high special resolution. Each map was acquired with a step size of 10 μm in x and y direction, a monochromator energy of 8950 eV, and a dwell time of 25 milliseconds. Acquired data were analyzed using *The MicroAnalysis Toolkit* software suite.[48] Quantification was carried out using custom Co standards with known concentrations coated on Mylar® films (MICROMATTER). Determined Co concentrations for each measurement spot (pixel) of a single sample were averaged in order to obtain a representative mean value, standard deviation, and error bars. For center regions, each pixel of the entire sample area was used for statistical calculations. For fold and edge regions, only pixels of the respective fold and pixels of the edge (without anode overhang) were considered for statistical calculations.

Synchrotron soft X-ray absorption spectroscopy:

Small pieces of harvested anodes and powdery CoO were applied on conductive carbon tape, which was then attached to an aluminum sample holder inside an argon filled glovebox (O_2 < 0.1 ppm, H_2O < 0.1 ppm). The rod was then packed into pouch bag and sealed inside the glove box prior to transportation.

Transfer into the ultrahigh vacuum chamber at the beam line was done under argon atmosphere to prevent any exposure to air. Soft XAS spectra of the Co L-edge were obtained at the 31-pole wiggler beam line 10-1 at the Stanford Synchrotron Radiation Lightsource (SSRL) with a spherical grating monochromator with 20 mm entrance and exit slits, a 0.2 eV energy resolution and a 2 x 2 mm beam spot. Data collection was performed under ultrahigh vacuum (10^{-9} Torr) at room temperature. All data were collected in a single load using the total electron yield (TEY) and fluorescence yield (FY) mode detectors. Data was processed using the Python multichannel analyzer (PyMCA) software of the European Synchrotron Radiation Facility (ESRF).[49]

Supporting Information

Pictures of harvested anodes from cell type A; X-ray diffraction and Raman spectra of locations with deposits; Contrast SEM-EDS images with total deposit coverage; Average concentration of Co depositions after different fast-charging protocols in center, folds, and edges; Schematic overview of Co deposition gradients on electrode edges; Soft X-ray absorption analysis of Co^{2+} deposits on anode; Optical image of cell type C anode.

References

(1)   Blomgren, G. E. The Development and Future of Lithium Ion Batteries. *J. Electrochem. Soc.* **2017**, *164* (1), A5019–A5025. https://doi.org/10.1149/2.0251701jes.

(2)   Takeuchi, T.; Kyuna, T.; Morimoto, H.; Tobishima, S. Influence of Surface Modification of LiCoO2 by Organic Compounds on Electrochemical and Thermal Properties of Li/LiCoO2 Rechargeable Cells. *J. Power Sources* **2011**, *196* (5), 2790–2801. https://doi.org/10.1016/j.jpowsour.2010.11.064.

(3)   Wang, L.; Ma, J.; Wang, C.; Yu, X.; Liu, R.; Jiang, F.; Sun, X.; Du, A.; Zhou, X.; Cui, G. A Novel Bifunctional Self-Stabilized Strategy Enabling 4.6 V LiCoO2 with Excellent Long-Term Cyclability and High-Rate Capability. *Adv. Sci.* **2019**, *6* (12), 1900355. https://doi.org/10.1002/advs.201900355.

(4)   Sun, Y.; Han, J.; Myung, S.; Lee, S.; Amine, K. Significant Improvement of High Voltage Cycling Behavior AlF3-Coated LiCoO2 Cathode. *Electrochem. commun.* **2006**, *8* (5), 821–826. https://doi.org/10.1016/j.elecom.2006.03.040.

(5)   Kim, Y.; Veith, G. M.; Nanda, J.; Unocic, R. R.; Chi, M.; Dudney, N. J. High Voltage Stability of LiCoO2 Particles with a Nano-Scale Lipon Coating. *Electrochim. Acta* **2011**, *56* (19), 6573–6580. https://doi.org/10.1016/j.electacta.2011.03.070.

(6)   Wu, S.; Lin, Y.; Xing, L.; Sun, G.; Zhou, H.; Xu, K.; Fan, W.; Yu, L.; Li, W. Stabilizing LiCoO2 / Graphite at High Voltages with an Electrolyte Additive. *ACS Appl. Mater. Interfaces* **2019**, *11* (19), 17940–17951. https://doi.org/10.1021/acsami.9b01053.

(7)   Chebiam, R. .; Kannan, a. .; Prado, F.; Manthiram, A. Comparison of the Chemical Stability of the High Energy Density Cathodes of Lithium-Ion Batteries. *Electrochem. commun.* **2001**, *3* (11), 624–627. https://doi.org/10.1016/S1388-2481(01)00232-6.

(8)   Amatucci, G. G.; Tarascon, J. M.; Klein, L. C. Cobalt Dissolution in LiCoO$_{2}$-Based Non-Aqueous Rechargeable Batteries. *Solid State Ionics* **1996**, *83* (1–2), 167–173. https://doi.org/10.1016/0167-2738(95)00231-6.

(9)   Lee, K. S.; Myung, S. T.; Kim, D. W.; Sun, Y. K. AlF3-Coated LiCoO2 and Li[Ni1/3Co 1/3Mn1/3]O2 Blend Composite Cathode for Lithium Ion Batteries. *J. Power Sources* **2011**, *196* (16), 6974–6977. https://doi.org/10.1016/j.jpowsour.2010.11.014.

(10)   Shen, B.; Liu, Q.; Wang, L.; Yin, G.; Zuo, P.; Ma, Y.; Cheng, X.; Du, C.; Gao, Y. Mixed Lithium Ion and Electron Conducting LiAlPO3.93F1.07-Coated LiCoO2 Cathode with Improved Electrochemical Performance. *Electrochem. commun.* **2017**, *83* (August), 106–109. https://doi.org/10.1016/j.elecom.2017.09.002.

(11)   Dai, X.; Zhou, A.; Xu, J.; Yang, B.; Wang, L.; Li, J. Superior Electrochemical Performance of LiCoO2 Electrodes Enabled by Conductive Al2O3-Doped ZnO Coating via Magnetron Sputtering. *J. Power Sources* **2015**, *298*, 114–122. https://doi.org/10.1016/j.jpowsour.2015.08.031.

(12)   Tomaszewska, A.; Chu, Z.; Feng, X.; O'Kane, S.; Liu, X.; Chen, J.; Ji, C.; Endler, E.; Li, R.; Liu, L.; et al. Lithium-Ion Battery Fast Charging: A Review. *eTransportation* **2019**, *1*, 100011. https://doi.org/10.1016/j.etran.2019.100011.

(13)   Li, W. Review—An Unpredictable Hazard in Lithium-Ion Batteries from Transition Metal Ions: Dissolution from Cathodes, Deposition on Anodes and Elimination Strategies. *J. Electrochem.*

Soc. **2020**, *167* (9), 090514. https://doi.org/10.1149/1945-7111/ab847f.

(14)   Zhan, C.; Wu, T.; Lu, J.; Amine, K. Dissolution, Migration, and Deposition of Transition Metal Ions in Li-Ion Batteries Exemplified by Mn-Based Cathodes – a Critical Review. *Energy Environ. Sci.* **2018**, *11* (2), 243–257. https://doi.org/10.1039/C7EE03122J.

(15)   Xu, M.; Wang, R.; Zhao, P.; Wang, X. Fast Charging Optimization for Lithium-Ion Batteries Based on Dynamic Programming Algorithm and Electrochemical-Thermal-Capacity Fade Coupled Model. *J. Power Sources* **2019**, *438* (June), 227015. https://doi.org/10.1016/j.jpowsour.2019.227015.

(16)   Anseán, D.; García, V. M.; González, M.; Viera, J. C.; Antón, J. C.; Blanco, C. Efficient Fast-Charging Strategies for Li-Ion Batteries. In *EVS28 International Electric Vehicle Symposium and Exhibition*; 2015.

(17)   Klein, R.; Chaturvedi, N. A.; Christensen, J.; Ahmed, J.; Findeisen, R.; Kojic, A. Optimal Charging Strategies in Lithium-Ion Battery. In *Proceedings of the 2011 American Control Conference*; IEEE, 2011; pp 382–387. https://doi.org/10.1109/ACC.2011.5991497.

(18)   Besli, M. M.; Subbaraman, A.; Pour Safaei, F. R.; Johnston, C.; Schneider, G.; Ravi, N.; Christensen, J.; Liu, Y.; Doeff, M. M.; Metzger, M.; et al. A Study of Model-Based Protective Fast-Charging and Associated Degradation in Commercial Smartphone Cells: Insights on Cathode Degradation as a Result of Lithium Depositions on the Anode. *Adv. Energy Mater.* **2021**, *11* (12), 2003019. https://doi.org/10.1002/aenm.202003019.

(19)   Komaba, S.; Kumagai, N.; Kataoka, Y. Influence of Manganese(II), Cobalt(II), and Nickel(II) Additives in Electrolyte on Performance of Graphite Anode for Lithium-Ion Batteries. *Electrochim. Acta* **2002**, *47* (8), 1229–1239. https://doi.org/10.1016/S0013-4686(01)00847-7.

(20)   Aurbach, D.; Markovsky, B.; Salitra, G.; Markevich, E.; Talyossef, Y.; Koltypin, M.; Nazar, L.; Ellis, B.; Kovacheva, D. Review on Electrode-Electrolyte Solution Interactions, Related to Cathode Materials for Li-Ion Batteries. *J. Power Sources* **2007**, *165* (2), 491–499. https://doi.org/10.1016/j.jpowsour.2006.10.025.

(21)   Zhan, C.; Wu, T.; Lu, J.; Amine, K. Dissolution, Migration, and Deposition of Transition Metal Ions in Li-Ion Batteries Exemplified by Mn-Based Cathodes-A Critical Review. *Energy Environ. Sci.* **2018**, *11* (2), 243–257. https://doi.org/10.1039/c7ee03122j.

(22)   Pieczonka, N. P. W.; Liu, Z.; Lu, P.; Olson, K. L.; Moote, J.; Powell, B. R.; Kim, J. H. Understanding Transition-Metal Dissolution Behavior in LiNi 0.5Mn1.5O4 High-Voltage Spinel for Lithium Ion Batteries. *J. Phys. Chem. C* **2013**, *117* (31), 15947–15957. https://doi.org/10.1021/jp405158m.

(23)   Aoshima, T.; Okahara, K.; Kiyohara, C.; Shizuka, K. Mechanisms of Manganese Spinels Dissolution and Capacity Fade at High Temperature. *J. Power Sources* **2001**, *97–98*, 377–380. https://doi.org/10.1016/S0378-7753(01)00551-1.

(24)   Thompson, L. M.; Stone, W.; Eldesoky, A.; Smith, N. K.; McFarlane, C. R. M.; Kim, J. S.; Johnson, M. B.; Petibon, R.; Dahn, J. R. Quantifying Changes to the Electrolyte and Negative Electrode in Aged NMC532/Graphite Lithium-Ion Cells. *J. Electrochem. Soc.* **2018**, *165* (11), A2732–A2740. https://doi.org/10.1149/2.0721811jes.

(25)   Wandt, J.; Freiberg, A.; Thomas, R.; Gorlin, Y.; Siebel, A.; Jung, R.; Gasteiger, H. A.; Tromp, M.

Transition Metal Dissolution and Deposition in Li-Ion Batteries Investigated by Operando X-Ray Absorption Spectroscopy. *J. Mater. Chem. A* **2016**, *4* (47), 18300–18305. https://doi.org/10.1039/C6TA08865A.

(26) Evertz, M.; Horsthemke, F.; Kasnatscheew, J.; Börner, M.; Winter, M.; Nowak, S. Unraveling Transition Metal Dissolution of Li1.04Ni1/3Co1/3Mn1/3O2 (NCM 111) in Lithium Ion Full Cells by Using the Total Reflection X-Ray Fluorescence Technique. *J. Power Sources* **2016**, *329*, 364–371. https://doi.org/10.1016/j.jpowsour.2016.08.099.

(27) Evertz, M.; Lürenbaum, C.; Vortmann, B.; Winter, M.; Nowak, S. Development of a Method for Direct Elemental Analysis of Lithium Ion Battery Degradation Products by Means of Total Reflection X-Ray Fluorescence. *Spectrochim. Acta - Part B At. Spectrosc.* **2015**, *112*, 34–39. https://doi.org/10.1016/j.sab.2015.08.005.

(28) Evertz, M.; Kröger, T. N.; Winter, M.; Nowak, S. Total Reflection X-Ray Fluorescence in the Field of Lithium Ion Batteries – Elemental Detection in Lithium Containing Electrolytes Using Nanoliter Droplets. *Spectrochim. Acta - Part B At. Spectrosc.* **2018**, *149* (January), 118–123. https://doi.org/10.1016/j.sab.2018.07.027.

(29) Menzel, M.; Schlifke, A.; Falk, M.; Janek, J.; Fröba, M.; Fittschen, U. E. A. Surface and In-Depth Characterization of Lithium-Ion Battery Cathodes at Different Cycle States Using Confocal Micro-X-Ray Fluorescence-X-Ray Absorption near Edge Structure Analysis. *Spectrochim. Acta - Part B At. Spectrosc.* **2013**, *85*, 62–70. https://doi.org/10.1016/j.sab.2013.04.001.

(30) Boesenberg, U.; Falk, M.; Ryan, C. G.; Kirkham, R.; Menzel, M.; Janek, J.; Fröba, M.; Falkenberg, G.; Fittschen, U. E. A. Correlation between Chemical and Morphological Heterogeneities in LiNi0.5Mn1.5O4 Spinel Composite Electrodes for Lithium-Ion Batteries Determined by Micro-X-Ray Fluorescence Analysis. *Chem. Mater.* **2015**, *27* (7), 2525–2531. https://doi.org/10.1021/acs.chemmater.5b00119.

(31) Ahmed, S.; Bloom, I.; Jansen, A. N.; Tanim, T.; Dufek, E. J.; Pesaran, A.; Burnham, A.; Carlson, R. B.; Dias, F.; Hardy, K.; et al. Enabling Fast Charging – A Battery Technology Gap Assessment. *J. Power Sources* **2017**, *367*, 250–262. https://doi.org/10.1016/j.jpowsour.2017.06.055.

(32) Ramezan Pour Safaei, F.; Subbaraman, A.; Ravi, N.; Klein, R.; Schmidt, G. S.; Cheng, Y. Method for Approximating Algorithms for Fast Charging Li-Ion Batteries Based on Electrochemical Battery Models. **2018**, US Patent No.: US20200150185A1.

(33) Chaturvedi, N.; Klein, R.; Christensen, J. F.; Ahmed, J.; Kojic, A. System and Method for Fast Charging of Lithium-Ion Batteries with Improved Safety. **2013**, US Patent No.: US9153991B2.

(34) Christensen, J. F.; Klein, R.; Krupadanam, A.; Mirtabatabaei, A.; Ravi, N. Staircase Charging. **2016**, US Patent No.: US20170338666A1.

(35) Bugga, R. V.; Smart, M. C. Lithium Plating Behavior in Lithium-Ion Cells. *ECS Trans.* **2010**, *25* (36), 241–252. https://doi.org/10.1149/1.3393860.

(36) Hein, S.; Latz, A. Influence of Local Lithium Metal Deposition in 3D Microstructures on Local and Global Behavior of Lithium-Ion Batteries. *Electrochim. Acta* **2016**, *201*, 354–365. https://doi.org/10.1016/j.electacta.2016.01.220.

(37) Waldmann, T.; Hogg, B. I.; Wohlfahrt-Mehrens, M. Li Plating as Unwanted Side Reaction in Commercial Li-Ion Cells – A Review. *J. Power Sources* **2018**, *384* (November 2017), 107–124.

https://doi.org/10.1016/j.jpowsour.2018.02.063.

(38)   Kozen, A. C.; Pearse, A. J.; Lin, C.-F.; Schroeder, M. A.; Noked, M.; Lee, S. B.; Rubloff, G. W. Atomic Layer Deposition and in Situ Characterization of Ultraclean Lithium Oxide and Lithium Hydroxide. *J. Phys. Chem. C* **2014**, *118* (48), 27749–27753. https://doi.org/10.1021/jp509298r.

(39)   Schneider, C. A.; Rasband, W. S.; Eliceiri, K. W. NIH Image to ImageJ: 25 Years of Image Analysis. *Nat. Methods* **2012**, *9* (7), 671–675. https://doi.org/10.1038/nmeth.2089.

(40)   Tang, M.; Albertus, P.; Newman, J. Two-Dimensional Modeling of Lithium Deposition during Cell Charging. *J. Electrochem. Soc.* **2009**, *156* (5), A390. https://doi.org/10.1149/1.3095513.

(41)   Verbrugge, M. W.; Baker, D. R. The Influence of Surface Inhomogeneity on the Overcharge and Lithium Plating of Graphite Electrodes. *J. Phys. Energy* **2019**, *2* (1), 014004. https://doi.org/10.1088/2515-7655/ab4dc1.

(42)   Fuchs, G.; Willenberg, L.; Ringbeck, F.; Sauer, D. U. Post-Mortem Analysis of Inhomogeneous Induced Pressure on Commercial Lithium-Ion Pouch Cells and Their Effects. *Sustain.* **2019**, *11* (23), 1–13. https://doi.org/10.3390/su11236738.

(43)   Bach, T. C.; Schuster, S. F.; Fleder, E.; Müller, J.; Brand, M. J.; Lorrmann, H.; Jossen, A.; Sextl, G. Nonlinear Aging of Cylindrical Lithium-Ion Cells Linked to Heterogeneous Compression. *J. Energy Storage* **2016**, *5*, 212–223. https://doi.org/10.1016/j.est.2016.01.003.

(44)   Ringbeck, F.; Rahe, C.; Fuchs, G.; Sauer, D. U. Identification of Lithium Plating in Lithium-Ion Batteries by Electrical and Optical Methods. *J. Electrochem. Soc.* **2020**, *167* (9), 090536. https://doi.org/10.1149/1945-7111/ab8f5a.

(45)   Ramanujapuram, A.; Gordon, D.; Magasinski, A.; Ward, B.; Nitta, N.; Huang, C.; Yushin, G. Degradation and Stabilization of Lithium Cobalt Oxide in Aqueous Electrolytes. *Energy Environ. Sci.* **2016**, *9* (5), 1841–1848. https://doi.org/10.1039/c6ee00093b.

(46)   Jung, R.; Linsenmann, F.; Thomas, R.; Wandt, J.; Solchenbach, S.; Maglia, F.; Stinner, C.; Tromp, M.; Gasteiger, H. A. Nickel, Manganese, and Cobalt Dissolution from Ni-Rich NMC and Their Effects on NMC622-Graphite Cells. *J. Electrochem. Soc.* **2019**, *166* (2), A378–A389. https://doi.org/10.1149/2.1151902jes.

(47)   Pourbaix, M. *Atlas of Electrochemical Equilibria in Aqueous Solutions*; National Association of Corrosion Engineers, 1974.

(48)   Webb, S. M.; McNulty, I.; Eyberger, C.; Lai, B. The MicroAnalysis Toolkit: X-Ray Fluorescence Image Processing Software. In *AIP Conference Proceedings*; 2011; Vol. 1365, pp 196–199. https://doi.org/10.1063/1.3625338.

(49)   Solé, V. A.; Papillon, E.; Cotte, M.; Walter, P.; Susini, J. A Multiplatform Code for the Analysis of Energy-Dispersive X-Ray Fluorescence Spectra. *Spectrochim. Acta - Part B At. Spectrosc.* **2007**, *62* (1), 63–68. https://doi.org/10.1016/j.sab.2006.12.002.